Title	Neutron quadrupole transition strength in $^{10}\mathrm{C}$ deduced from the $^{10}\mathrm{C}(\alpha,\alpha')$ measurement with the MAIKo active target
Author(s)	Furuno, T; Kawabata, T.; Adachi, S. et al.
Citation	Physical Review C. 2019, 100(5), p. 054322-054322
Version Type	VoR
URL	https://hdl.handle.net/11094/73730
rights	©2019 American Physical Society
Note	

Neutron quadrupole transition strength in ^{10}C deduced from the ^{10}C(α, α') measurement with the MAIKo active target

T. Furuno [1], T. Kawabata [2], S. Adachi,[3] Y. Ayyad [4], Y. Kanada-En'yo,[5] Y. Fujikawa,[5] K. Inaba,[5] M. Murata,[5,*]
H. J. Ong [1], M. Sferrazza,[6] Y. Takahashi,[5] T. Takeda [5], I. Tanihata [1,7] D. T. Tran [1,8] and M. Tsumura[5]

[1]*Research Center for Nuclear Physics (RCNP), Osaka University, Ibaraki, Osaka 567-0047, Japan*
[2]*Department of Physics, Osaka University, Toyonaka, Osaka 560-0043, Japan*
[3]*Department of Physics, Kyushu University, Fukuoka, Fukuoka 819-0395, Japan*
[4]*Facility for Rare Isotope Beams (FRIB), Michigan State University, East Lansing, Michigan 48824, USA*
[5]*Department of Physics, Kyoto University, Sakyo, Kyoto 606-8502, Japan*
[6]*Départment de Physique, Université Libre de Bruxelles, Bruxelles 1050, Belgium*
[7]*International Research Center for Nuclei and Particles in the Cosmos, and School of Physics and Nuclear Energy Engineering, Beihang University, Beijing 100191, China*
[8]*Institute of Physics, Vietnam Academy of Science and Technology, BaDinh, Hanoi 100000, Vietnam*

Elastic and inelastic alpha scatterings on ^{10}C were measured using a 68-MeV/u radioactive ^{10}C beam incident on the recently developed MAIKo active target system. The phenomenological effective α-N interaction and the point-nucleon density distribution in the ground state were determined from the elastic scattering data. The cross sections of the inelastic alpha scattering were calculated using this interaction and density distribution and were compared with the experiment to determine the neutron quadrupole transition matrix element M_n between the ground state and the 2_1^+ state at $E_x = 3.35$ MeV in ^{10}C. The deduced neutron transition matrix element is $M_n = 6.9 \pm 0.7$ (fit) ± 1.2 (sys) fm^2. The ratio of the neutron transition strength to proton transition strength was determined as $M_n/M_p = 1.05 \pm 0.11$ (fit) ± 0.17 (sys), which indicates that the quadrupole transition between the ground state and the 2_1^+ state in ^{10}C is less neutron dominant compared to that in ^{16}C.

I. INTRODUCTION

Quadrupole transitions between nuclear states provide valuable insight into nuclear structure. Their strengths are key benchmarks in testing theoretical models. In particular, the quadrupole transition strengths from the ground (0_1^+) state to the 2_1^+ state in even-even nuclei reflect nuclear shell structures [1–5]. The quadrupole transitions are described as rearrangements of particle-hole configurations in the valence shells under the framework of the nuclear shell model. When the neutron (proton) shell is closed, the transition of the neutron (proton) is suppressed remarkably because the intrashell excitation in the closed shell is forbidden. As a consequence, the ratio of the neutron and proton transition strengths deviates from unity.

The neutron (proton) transition matrix element from the 0_1^+ state to the 2_1^+ state is defined as follows:

$$M_{n(p)} = \langle 2_1^+ || \sum_{n(p)} r^2 Y_2 || 0_1^+ \rangle. \qquad (1)$$

Here, Y_2 represent the spherical functions for $L = 2$. Considering the proton as a point particle, M_p can be related to the reduced electric quadrupole transition rate $B(E2; 0_1^+ \to 2_1^+)$ by the following relation:

$$B(E2; 0_1^+ \to 2_1^+) = e^2 |M_p|^2. \qquad (2)$$

The relationship between excitation ($0_1^+ \to 2_1^+$) and deexcitation ($2_1^+ \to 0_1^+$) reduced transition rates can be given by a simple equation

$$\begin{aligned} B(E2; 0_1^+ \to 2_1^+) &= \frac{2J'+1}{2J+1} B(E2; 2_1^+ \to 0_1^+) \\ &= 5B(E2; 2_1^+ \to 0_1^+), \end{aligned} \qquad (3)$$

where J and J' are the spins of the ground and excited states.

There is no direct way to determine M_n since there exists no probe that is sensitive only to neutrons. To determine M_n of a nucleus, one can either adopt M_p of its mirror nucleus assuming charge symmetry, or disentangle M_n from inelastic scattering cross sections using a hadronic probe such as a proton or alpha particle, incorporating M_p obtained from the $B(E2; 0_1^+ \to 2_1^+)$ value.

With the progress on techniques for providing radioactive isotope (RI) beams over the past few decades, numerous efforts have been made to deduce transition matrix elements in unstable nuclei [6–30]. The highlights are the discovery of the enhanced M_n/M_p ratio and the suppression of M_p in neutron-rich carbon isotopes. The M_n/M_p ratio in ^{16}C is as

---

*Present address: Research Center for Nuclear Physics (RCNP), Osaka University, Ibaraki, Osaka 567-0047, Japan.

large as 3 [11,16,20], which is much larger than $N/Z = 1.7$. The reduced electric quadrupole transition rates $B(E2; 2_1^+ \to 0_1^+)$ in ^{16}C [12,19,20,23], ^{18}C [20,24], and ^{20}C [22] are small, i.e., approximately 1.1–2.3 Weisskopf units (W.u.).

In Ref. [31], the large M_n/M_p ratio or quenching of M_p in neutron-rich carbon isotopes was attributed to the subshell closure at $Z = 6$. It is of interest to see whether the large M_n/M_p ratio is observed in a proton-rich carbon isotope as well, for example, ^{10}C.

The $B(E2; 2_1^+ \to 0_1^+)$ value in ^{10}C had been known to be 9.6 ± 1.6 W.u. [32]. This value is not small as compared to those in the neutron-rich carbon isotopes. From an inelastic proton scattering experiment [13], the M_n/M_p ratio in ^{10}C was measured to be 0.70 ± 0.08, which is not so large compared to that in neutron-rich ^{16}C. However, a more recent lifetime measurement on the 2_1^+ state in ^{10}C reported a smaller value of $B(E2; 2_1^+ \to 0_1^+) = 6.9 \pm 0.2$ W.u. [33] with uncertainty much smaller in comparison with the previous measurement. Therefore, it is important to revisit the M_n/M_p ratio in ^{10}C. To determine M_n in ^{10}C, instead of the inelastic proton scattering, we utilized the inelastic alpha scattering, which is an isoscalar probe.

In order to determine the neutron matrix element M_n from the cross section of the inelastic hadron scattering, the Bernstein prescription $d\sigma/d\Omega \propto |b_n^F M_n + b_p^F M_p|^2$ is often used [2]. Here, b_n^F and b_p^F are external-field interaction strengths that reflect the effective interaction between an incident particle and a proton or neutron in nuclei. In the case of (p, p') scattering, the ratio b_n/b_p is phenomenologically determined. However, this ratio has a strong energy dependence; it varies from 3 to 0.83 in the incident-energy range of 10–1000 MeV [3], and it also depends on the nucleus. This dependence causes a significant model ambiguity in the determination of the M_n/M_p ratio from (p, p') scattering. On the other hand, in (α, α') scattering, the b_n^F/b_p^F ratio is always unity because of the zero isospin of an alpha particle. Therefore, (α, α') scattering is more suited to deduce M_n than (p, p') scattering.

To deduce M_n from the measured cross section, distorted-wave Born-approximation (DWBA) calculations should be performed. Recently, the alpha inelastic scattering off the self-conjugate even-even nuclei from ^{12}C to ^{40}Ca was systematically measured [34]. The DWBA calculations using single-folding model potentials reasonably reproduce the measured cross sections, once the effective α-N interaction is determined to reproduce the elastic alpha scattering. Therefore, the cross sections of the elastic as well as inelastic alpha scattering should be measured.

Since ^{10}C is unstable, the measurement must be done in the inverse kinematic condition. One of the best methods to measure the cross sections of the elastic and inelastic scatterings in a single experiment is missing mass spectroscopy, in which the excitation energies of incoming nuclei are determined from energies and angles of recoil particles. In fact, the previous (p, p) and (p, p') measurements were performed using missing mass spectroscopy [13]. However, it is not easy to apply missing mass spectroscopy to alpha inelastic scattering, especially at low momentum transfer of $q \approx 0.5$ fm^{-1} where the differential cross section for the 2_1^+ state becomes maximum. Because the energies of the recoil alpha particles

are only $E_\alpha \approx 1$ MeV at $q \approx 0.5$ fm^{-1}, it is almost impossible to detect low-energy particles by a conventional experimental setup.

To overcome the challenge of detecting low-energy recoil alpha particles, we recently developed the MAIKo active target [35]. This system consists of a time projection chamber (TPC) which is a gaseous detector with three-dimensional reconstruction capability for charged particle trajectories. In the active target mode, the detection medium gas of the TPC is also used as the target gas. The detection of low-energy recoil particles becomes possible because the reaction occurs inside the sensitive volume of the TPC

In this paper, we report measurements of the cross sections for $\alpha + {}^{10}$C elastic and inelastic scatterings at an incident energy of 68 MeV/u. The present experiment is the first attempt to deduce the M_n value in unstable nuclei from (α, α') scattering and the first experiment using the MAIKo active target. The cross sections were measured at $\theta_{c.m.} = 45°$–$15°$, which corresponds to the momentum transfer of $q = 0.4$–1.4 fm^{-1}. The neutron transition matrix element M_n in ^{10}C was determined and the M_n/M_p ratio is discussed.

II. EXPERIMENT

The measurement was carried out at the cyclotron facility of Research Center for Nuclear Physics (RCNP), Osaka University. A ^{10}C secondary beam was produced via projectile fragmentation using a ^{12}C^{6+} primary beam at 96 MeV/u accelerated by the azimuthally varying field cyclotron and the ring cyclotron. The primary beam with intensities ranging from 50 to 100 p nA was transported to the exotic nuclei (EN) beamline shown in Fig. 1, and incident on a 450-mg/cm^2-thick ^{9}Be production target at the F0 focal plane. ^{10}C particles were separated from other fragments using the fragment separator at the EN beamline [36–38] by setting the appropriate magnetic rigidities in two dipole magnets (D1 and D2). To improve isotope separation, a 2-mm-thick aluminum degrader was placed at the first focal plane (F1). The ^{10}C beam was angular focused at the second focal plane (F2), which is a charge-mass dispersive focal plane, and further selected using a pair of collimators at F2. The selected ^{10}C beam was later transported to the third focal plane (F3) and injected into the MAIKo active target. During the tuning of the secondary beam, the purity of ^{10}C was measured from the correlation between the energy loss of the beam particles in a Si detector before MAIKo and the time of flight. The time of flight was measured between the F0 target and the Si detector using the radio-frequency signal from the accelerator. Because the purity of ^{10}C was as high as 96% before MAIKo, event-by-event beam particle identification (PID) was not necessary for the present work.

The details of the detector setup at F3 are shown in the inset of Fig. 1. The intensity of the beam was measured with a 1-mm-thick plastic scintillator (F3PL) placed downstream of MAIKo at F3. The typical beam intensity was 70 000 counts per second (cps). We placed two multiwire drift chambers (MWDCs) before MAIKo for monitoring the profile of the incident beam. The distance between the two MWDCs was 600 mm, and the distance from the downstream MWDC to
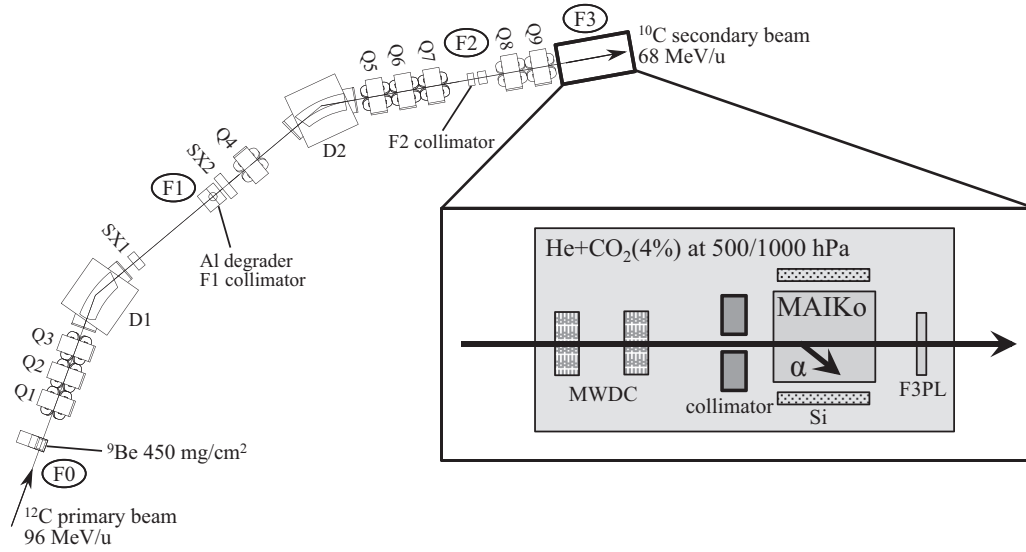
FIG. 1. Schematic view of the EN course and the beamline detectors. The inset shows the details of the detector setup at F3.

the entrance of MAIKo was 733 mm. The ^{10}C beam was horizontally collimated to ± 10 mm by 10-mm-thick tungsten collimators before MAIKo. The angular spread of the ^{10}C beam was 15 mrad in the horizontal direction and 6 mrad in the vertical direction. The spot size of the ^{10}C beam at the entrance of MAIKo was 5 mm both in horizontal and vertical directions. The average energy of the ^{10}C beam was 68 MeV/u before the F3PL with an energy spread of 1%.

Figure 2 shows the schematic view of the MAIKo active target. The TPC field cage has dimensions of $150 \times 150 \times 140$ mm^3. The angle from the beam axis and the kinetic energy of the recoil alpha particle are measured to determine the excitation energy of ^{10}C and the scattering angle in the center-of-mass (c.m.) frame. The recoil angle is determined from the reconstructed trajectory of the recoil alpha particle. The kinetic energy is determined from the length of the trajectory

when the recoil alpha particles stop in the sensitive volume of the TPC. High-energy recoil alpha particles that escape from the TPC sensitive volume are detected by four silicon detectors placed outside the TPC. Each silicon detector has a sensitive area of 90×60 mm^2, and a thickness of 500 μm. When a recoil alpha particle stops between the silicon detectors and the TPC, the recoil energy cannot be determined. Because the insensitive energy region depends on the gas pressure, the TPC was operated at two different gas pressures.

The TPC was operated with a He + CO$_2$(4%) mixture gas at 500 and 1000 hPa. When the gas pressure is 500 hPa, alpha particles with kinetic energies $E_\alpha < 1$ MeV stop in the sensitive volume of the TPC, while alpha particles with $E_\alpha > 4$ MeV reach the silicon detectors. When the gas pressure is at 1000 hPa, alpha particles with $E_\alpha < 3$ MeV stop inside the TPC.

The TPC shared the same gas chamber with the MWDCs, and thus the TPC and MWDCs were operated using the same detection gas. The He and CO$_2$ gasses were individually supplied using two mass flow controllers to keep the mixing ratio and the flow rate constant. The total flow rate was set at 100 cm^3/min. The pressure and the temperature inside the chamber were monitored using a diaphragm gauge and a Pt-100 thermometer, respectively. The gas density was determined from the pressure and temperature. The mixture gas was exhausted from the chamber using a scroll pump. A piezo valve was installed between the chamber and the pump. The aperture of the valve was automatically controlled to keep the gas density constant according to the measured pressure and temperature. The density fluctuation was within $\pm 0.2\%$ throughout the measurement.

The red arrows in Fig. 2 present trajectories of an incident ^{10}C, a scattered ^{10}C, and a recoil alpha particle. The ^{10}C nuclei and recoil alpha particles ionize the gas molecules along their trajectories. The ionized electrons drift vertically along the electric field formed by the TPC field cage. The electric field was formed by applying negative high voltages on the stainless-steel cathode plate and the nickel grid mesh.
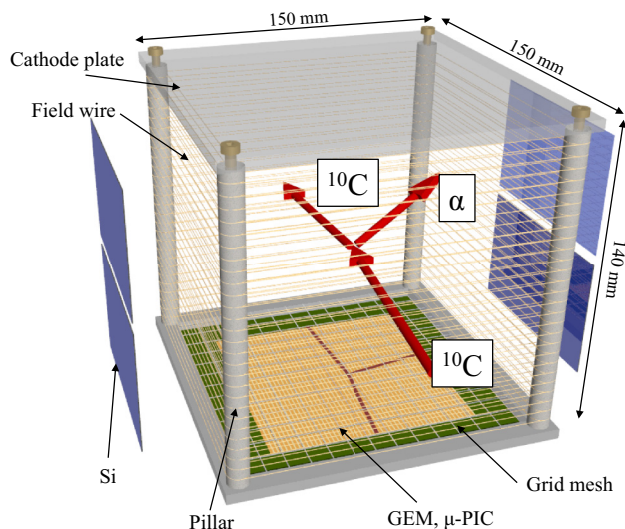

FIG. 2. Schematic view of the MAIKo active target.

The cathode plate and the grid mesh were kept at a distance of 140 mm by four pillars made of Macor ceramic. Field wires made of beryllium copper were doubly wound around the pillars with 5-mm intervals to make the electric field uniform. The strength of the electric field was chosen such that the electron-drift velocity was 1.7 cm/μs for both 500 and 1000 hPa pressures. The electron-drift velocity was measured using collimated alpha particles from a ^{241}Am source. The above drift velocity is high enough to collect the electrons from the full active volume, within the time window of 10.24 μs.

After the drifted electrons pass through the grid mesh, they are multiplied first through a gas electron multiplier (GEM) and then by a micro-pixel chamber (μ-PIC) [39]. The total gas gain of the GEM and the μ-PIC was measured to be about 870 in operation at 500 hPa. The μ-PIC was also used to measure the position of the drifted electrons. The μ-PIC has a sensitive area of 102.4×102.4 mm^2. It consists of 256 anode strips and 256 cathode strips which are arranged orthogonally. These strips are fabricated at 400-μm intervals. The signals induced by the electron avalanche are read out through the anode and cathode strips which provide the two-dimensional information of the particle trajectories. The vertical position of the trajectories are determined from the electron drift time multiplied by the drift velocity.

The analog signals from the anode and cathode strips are preamplified, shaped, and discriminated with dedicated readout boards [40]. The discriminators give output, a high or low-level signal, by comparing the pulse height of the shaped analog signal with a threshold voltage. The output of the discriminators is synchronized with a 100-MHz clock. When a trigger signal is provided to the readout boards, the status of the discriminators at every 10 ns is recorded as a function of the clock number for a time window of 10.24 μs. The summed pulse shapes of the adjacent 32 strips (12.8 mm width) are also recorded by 25-MHz flash analog-to-digital converters (FADCs).

The data recorded by the discriminators are equivalent to two black-and-white images with 256×1024 pixels. Each image presents particle trajectories projected onto the plane perpendicular to the anode or cathode strips. Examples of the track images of α + ^{10}C events are shown in Figs. 3 and 4. In Fig. 3, another ^{10}C entering the sensitive volume of MAIKo about 150 clocks (= 1.5 μs) before the scattering event was accidentally recorded. The ^{10}C beam trajectories appear as horizontal loci in the anode images because the anode strips are perpendicular to the beam axis. On the other hand, they appear as elliptical shapes in the cathode image because the cathode strips are parallel to the beam axis.

The trigger signal for the data acquisition was generated from the silicon detectors or cathode strips. To suppress the triggers due to the beam particles, the 65th–160th cathode strips were excluded from the trigger. This trick inhibits the shaded area in Figs. 3(b) and 4(b) from triggering data acquisition. When the beam intensity was 77 kHz and the gas pressure was at 500 hPa, the trigger rate was 270 Hz, and the live time ratio of the data acquisition was 88%.

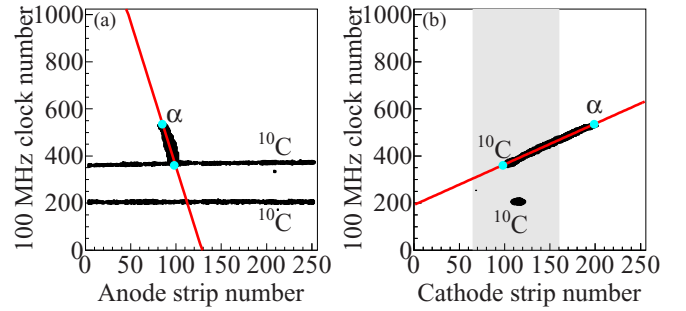In addition to the measurement using the ^{10}C beam, we also performed a similar measurement using the ^{12}C primary

FIG. 3. Example of (a) anode and (b) cathode images acquired in an α + ^{10}C event. The reconstructed trajectories of the recoil particle are drawn with the solid red lines. The vertex and the track endpoints are shown by the cyan circles. The shaded area in the cathode image was excluded from the trigger condition.

beam to compare the cross section measured by MAIKo with the previous result measured under the normal kinematic condition [34].

III. DATA REDUCTION

MAIKo acquired not only the α + ^{10}C scattering events but also background events. The background events were mainly caused by ^{10}C beam particles which invade the cathode trigger region (beam events). Scattering from the quenching CO_2 gas also caused the background events. The fraction of the α + ^{10}C events in the acquired events was only of the order of 1%. Therefore, the α + ^{10}C events must be correctly distinguished from the background events.

The α + ^{10}C events exhibit the following two features. First, energy losses per unit length of recoil alpha particles are about 7 times larger than those of ^{10}C beam particles. Second, because ^{10}C is much heavier than an alpha particle, the scattering hardly deflects ^{10}C; however, alpha particles recoil at large angles. Therefore, just one trajectory with a large angle from the horizontal line (nonhorizontal trajectory) due to a recoil alpha particle should be observed in the anode image, as seen in Figs. 3(a) and 4(a). On the other hand, in a beam event, the nonhorizontal trajectory is not recorded. In a
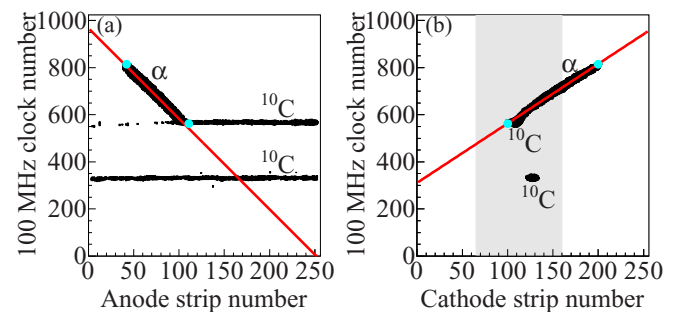

FIG. 4. Same as Fig. 3, but track images in an inelastic scattering event exciting a highly excited state above the proton decay threshold at $E_x = 3.82$ MeV. The trajectories of two protons and two alpha particles from the breakup of ^{10}C are thin because of the small energy loss.

background event due to the CO_2 gas, multiple nonhorizontal trajectories are observed.

Considering these features, the analysis of the TPC data was performed with the following procedures.

(i) Eliminate the hit pixels in the anode and cathode images from the analysis, where the corresponding induced charges measured with the FADCs are smaller than a certain threshold.

(ii) Extract the straight lines in the anode and cathode images using the Hough transformation [41,42] as described in Ref. [35].

(iii) If the number of nonhorizontal lines in the anode images is 1, this line is regarded as the trajectory of the recoil alpha particles. Fit the hit pixels near the trajectory of the recoil particle to a straight line for a better track determination. The fits are shown by the solid red lines in Figs. 3(a) and 4(a).

(iv) Ignore the straight lines in the cathode images shorter than a certain threshold to remove the trajectories of unreacted ^{10}C. If the number of the remaining straight lines is 1, fit the hit pixels to a straight line as done in anode images. The fits are shown by the solid red lines in Figs. 3(b) and 4(b).

(v) Find the vertex and track endpoints in the anode and cathode images along the fitted lines. These points are indicated with the cyan circles in Figs. 3 and 4.

(vi) From the angles of the straight lines in the anode and cathode images, calculate the polar and azimuthal recoil angles, assuming the beam axis is parallel to the cathode strips. The range of the recoil particle is determined from the distance between the vertex and the track endpoints.

We selected the $\alpha + {}^{10}C$ events where the vertex point locates between the 33rd–224th strips in the anode image. Thus, the effective length of MAIKo as a He gas target was 76.8 mm.

PID for the recoil particles must be performed. Ranges of charged particles in the gas are proportional to $E^2/(AZ^2)$, and total charges collected by the μ-PIC are proportional to kinetic energies of recoil particles, if the recoil particles stop in the sensitive volume of the TPC. Therefore, PID can be performed from the correlation between the total charge measured with the μ-PIC and the range, as shown in Fig. 5(a).

If recoil particles escape from the TPC and hit the silicon detectors, PID can be performed from the correlation between the charge collected by μ-PIC and the energy measured by the silicon detector, as shown in Fig. 5(b).

In both cases, the loci of the $Z = 2$ particles are clearly separated from the loci of $Z > 2$ and $Z = 1$ particles. We selected the $Z = 2$ events enclosed by the solid red lines in Fig. 5. The minimum range for the recoil alpha particle is 25 mm.

If recoil alpha particles stop inside the sensitive volume of the TPC, recoil energies are calculated from ranges in the gas using the SRIM code [43]. If recoil alpha particles hit the silicon detectors, recoil energies are calculated using $E_\alpha = E_{Si} + \Delta E_{gas}$, where E_{Si} is the energy measured with the
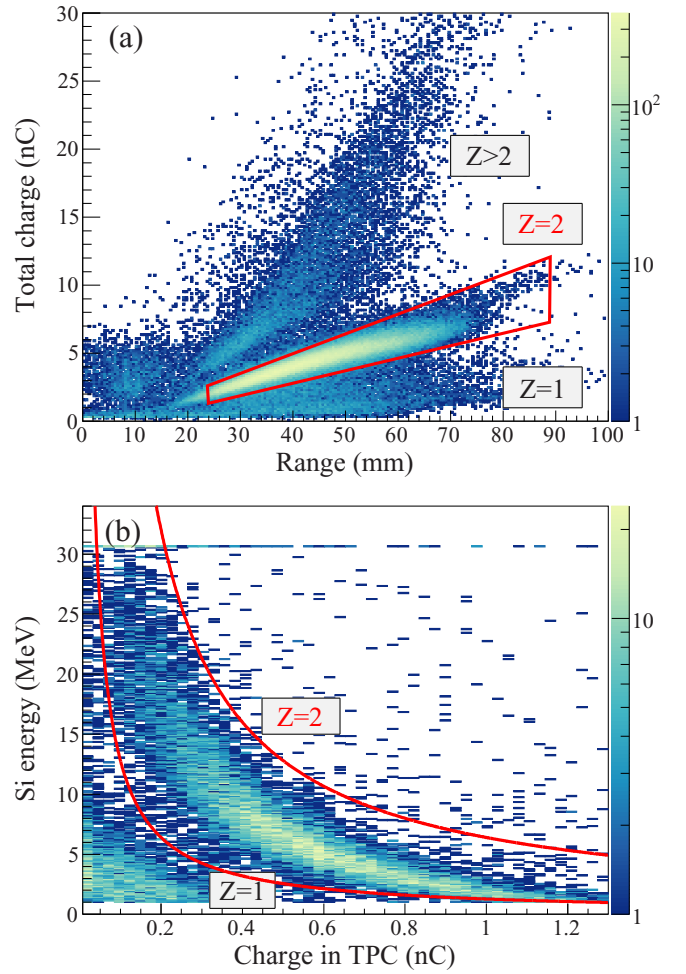

FIG. 5. PID of recoil particles in the measurement at 500 hPa. (a) Correlation between the total charge collected by the μ-PIC and the range of the recoil particle. (b) Correlation between the energy measured with a silicon detector and the charge collected with the 32 cathode strips near the silicon detector.

silicon detector and ΔE_{gas} is the energy loss of the recoil alpha particle in the gas. ΔE_{gas} is calculated by integrating dE/dx along the particle trajectory between the silicon detector and the vertex position.

Figure 6 shows the reconstructed recoil energy versus the recoil angle in the $\alpha + {}^{10}C$ events. The red and blue dots represent events in which a recoil alpha particle stopped inside the TPC during the measurements at 500 and 1000 hPa (denoted as "500 hPa event" and "1000 hPa event"), respectively. The green dots represent events in which a recoil alpha particle hit one of the silicon detectors during the measurement at 500 hPa (denoted as "Si event"). With the present measurement, we successfully lowered the detection threshold to 0.5 MeV. This detection threshold is determined by the minimum range of 25 mm defined in the PID procedure. The calculated energies and angles of recoil alpha particles at different excitation energies in ^{10}C are shown with the solid lines.

Excited states in ^{10}C below the proton emission threshold at $E_x = 3.82$ MeV always decay to the ground state by
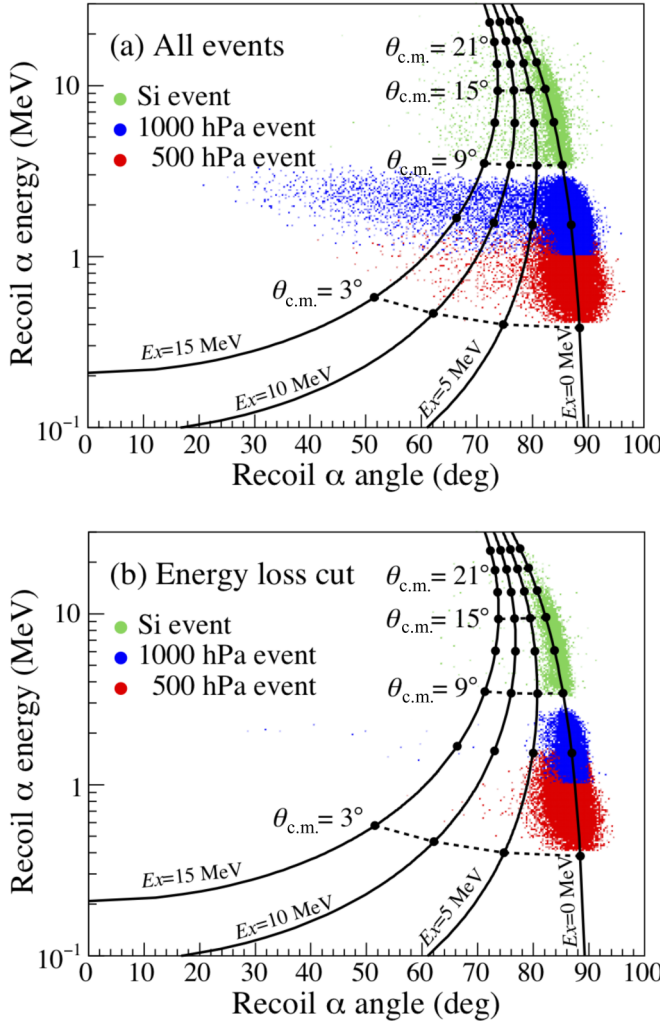
FIG. 6. Scatter plots of kinematic energies versus angles of recoil alpha particles. (a) All of the $\alpha + {}^{10}C$ events. (b) The elastic and inelastic scattering events to low excited states selected by the FADC data. The red, blue, and green dots show the "500 hPa," "1000 hPa," and "Si" events, respectively. Kinematically calculated energies and angles of recoil alpha particles at different excitation energies in ${}^{10}C$ are shown by the solid lines.

emitting a γ ray. Because both the incident and scattered particles are ${}^{10}C$, the energy loss of ${}^{10}C$ per unit length in the TPC gas after the scattering point is almost the same as that before the scattering point. Therefore, thicknesses of the observed horizontal trajectories in the anode image look similar before and after the scattering point, as seen in Fig. 3(a). On the other hand, when the excitation energy is above the proton emission threshold, the excited states immediately decay into $2p + 2\alpha$ particles. Since energy loss of the $2p + 2\alpha$ particles is about $1/3$ of the incident ${}^{10}C$, the observed horizontal trajectories after the scattering point look thinner than before the scattering point, as seen in Fig. 4(a). Therefore, inelastic scattering to highly excited states at $E_x > 3.82$ MeV is easily discriminated from the elastic scattering and inelastic scattering to low excited states at $E_x < 3.82$ MeV by using the energy-loss information obtained from the most downstream channel of
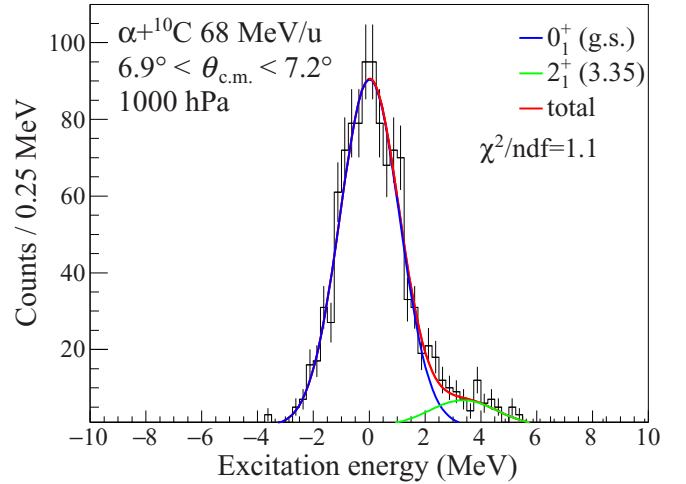

FIG. 7. Excitation energy spectrum in the $\alpha + {}^{10}C$ scattering at $E = 68$ MeV/u and $6.9° < \theta_{c.m.} < 7.2°$. The solid lines represent the fit result of 0_1^+ (blue), 2_1^+ (green), and sum of the two states (red), respectively.

the FADC for the 1st–32nd anode strips. Figure 6(a) includes all of the $\alpha + {}^{10}C$ events, while Fig. 6(b) includes the elastic and inelastic scattering events to low excited states selected by the FADC data. Using energy loss information, only low-lying states below the particle decay threshold were successfully selected. In the present work, we focus on the low-excitation energy events.

Figure 7 shows the excitation-energy spectrum in the $\alpha + {}^{10}C$ scattering at $E = 68$ MeV/u and $6.9° < \theta_{c.m.} < 7.2°$. A prominent peak due to the ground state is observed with a small contribution from the 2_1^+ state at $E_x = 3.35$ MeV. The resolutions of the excitation energy for the ground state and the c.m. angle are $\Delta E_x = 1$ MeV and $\Delta\theta_{c.m.} = 0.07°$ in sigma, respectively. The excitation-energy resolution is limited mainly due to the angular straggling of recoil alpha particles in the TPC gas. As an example, angles of alpha particles at 2 MeV are straggled about 30 mrad due to collisions with the gas particles at 1000 hPa. By fitting the spectrum with two Gaussians, the yields of the ground and 2_1^+ states were obtained. At $\theta_{c.m.} < 5°$, the yield of the 2_1^+ state could not be determined because the contribution of the 2_1^+ state was much smaller than that of the ground state.

The detection efficiency for the present measurement was estimated by a Monte Carlo simulation. It was assumed that the $\alpha + {}^{10}C$ scattering occurs inside the sensitive volume of the TPC over the entire solid angle. Primary electrons were generated along the ${}^{10}C$ and recoil alpha trajectories according to the SRIM calculation, considering the angular straggling of the recoil alpha particles. These electrons drifted towards the μ-PIC. The transverse and longitudinal diffusions of the electrons were taken into account. The charge collection rate by the μ-PIC as a function of time was folded by the response function of the readout circuit to simulate the analog signal from each strip. The simulated signals were virtually processed and the track images were generated. These images were analyzed in the same manner as the real data. The number of reconstructed events at each $\theta_{c.m.}$ and E_x was divided
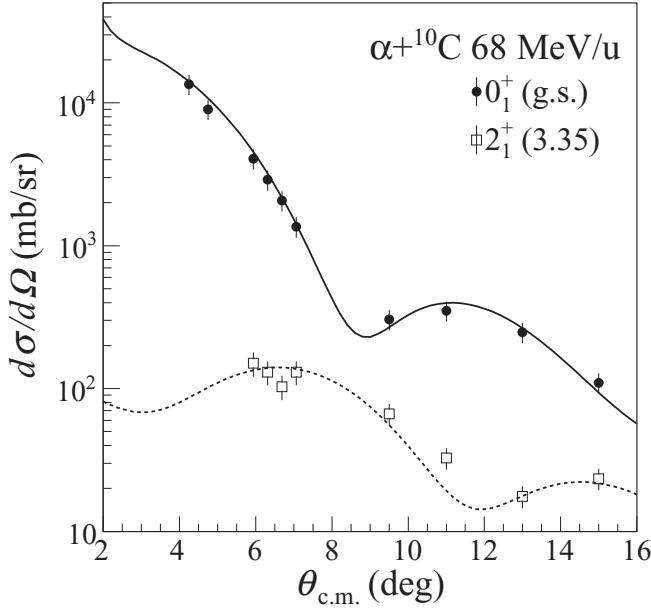
FIG. 8. Differential cross sections for the $\alpha + {}^{10}$C elastic (solid circles) and inelastic scatterings to the 2_1^+ state at $E_x = 3.35$ MeV (open squares). The cross section of the elastic scattering calculated with the optical-model potential is shown by the solid line, while the cross section of the inelastic scattering obtained by the DWBA calculation is shown by the dashed line.
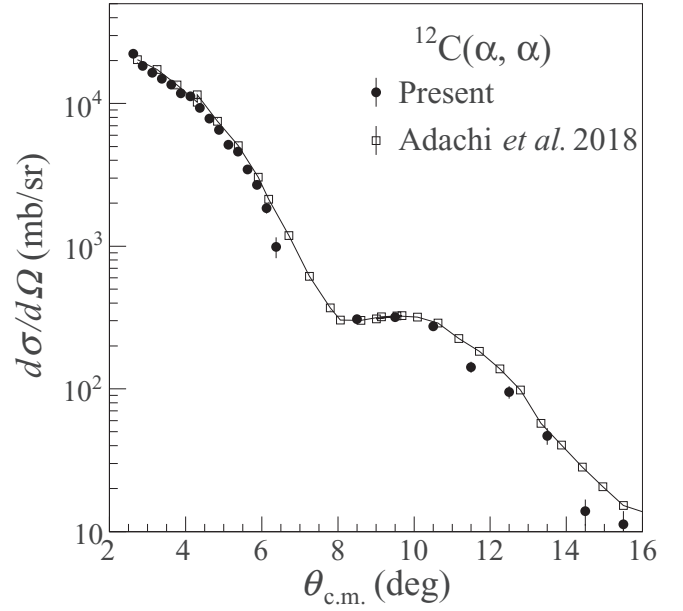

FIG. 9. Differential cross sections for the $\alpha + {}^{12}$C elastic scattering at 94 MeV/u (solid circles) compared with the previous results measured under the normal kinematic condition at 96 MeV/u (open squares) [34]. The solid line connecting the open squares is drawn to guide the eyes.

by the number of generated events to estimate the detection efficiency. The efficiency depends on the recoil angle and energy in the laboratory frame. For example, when the recoil alpha particles are emitted to $\theta_{\text{lab.}} = 88°$ with an energy of 0.8 MeV, which corresponds to $\theta_{\text{c.m.}} = 4.5°$ and $E_x = 0$ MeV, the efficiency for the alpha particles to reach the trigger region, and to start the data acquisition, is about 36%. The track reconstruction efficiency for the recorded events is about 82%. Consequently, the total efficiency is about 30%.

Finally, the differential cross sections of the $\alpha + {}^{10}$C elastic scattering and the inelastic scattering exciting the 2_1^+ state at $E_x = 3.35$ MeV were obtained, as plotted in Fig. 8. The cross section of the $\alpha + {}^{12}$C elastic scattering is also obtained to check the present analysis. In Fig. 9 the measured cross section is compared with the previous result obtained using a ^{4}He beam at 96 MeV/u under the normal kinematic condition [34]. The present result agrees with the previous result qualitatively; however, it is systematically smaller than the previous result by 10% on average. The normalization factors of the present result to the previous result at different angles fluctuate $\pm 16\%$ around the averaged value. This is mainly due to the uncertainty of the detection efficiency of MAIKo. Therefore, we added 16% fractional uncertainty to the statistical uncertainty in quadrature in the following analysis.

IV. ANALYSIS

We performed the DWBA calculation with single-folding potentials to extract the neutron transition matrix element M_n in ^{10}C from the cross section of the alpha inelastic scattering to the 2_1^+ state. The phenomenological α-N effective interaction

and the ground-state density distribution were determined to reproduce the cross section of the alpha elastic scattering. The DWBA calculations were performed using the computer code ECIS-95 [44].

A. Analysis of alpha elastic scattering

The optical-model potential for the $\alpha + {}^{10}$C elastic scattering was obtained by folding a phenomenological α-N effective interaction u with the point-nucleon distribution in the ground state $\rho(\mathbf{r}')$:

$$U(r) = \int \rho(\mathbf{r}')u[|\mathbf{r} - \mathbf{r}'|, \, \rho(\mathbf{r}')]d\mathbf{r}', \qquad (4)$$

where $\mathbf{r}$ and $\mathbf{r}'$ represent the positions of the alpha particle and nucleons in ^{10}C, respectively. The phenomenological α-N interaction was parametrized as given in Ref. [34]:

$$u[|\mathbf{r} - \mathbf{r}'|, \, \rho(\mathbf{r}')] = -V[1 + \beta\rho^{2/3}(\mathbf{r}')]e^{-|\mathbf{r}-\mathbf{r}'|^2/\alpha_V^2}$$
$$- iW[1 + \beta\rho^{2/3}(\mathbf{r}')]e^{-|\mathbf{r}-\mathbf{r}'|^2/\alpha_W^2}. \quad (5)$$

The parameters V and W are the depths of the real and imaginary potentials, respectively. β is the density-dependent coefficient of the interaction. α_V and α_W are the range parameters of the real and imaginary parts. In the present analysis, we assumed that the real and imaginary ranges are the same ($\alpha_V = \alpha_W = \alpha$) and the interaction is density-independent ($\beta = 0$). It was reported that the density-dependent ($\beta \neq 0$) and density-independent interactions provide almost the same cross sections for the 2_1^+ states in the DWBA calculation once the interaction parameters are determined to reproduce the

TABLE I. Optimized parameters for the α-N effective interaction and the point-nucleon distribution of the ground state in ^{10}C in the present analysis.

	Interaction			3pG		
α (fm)	V (MeV)	W (MeV)	c (fm)	z (fm)	w	rms (fm)
2.13	$25.8^{+3.1}_{-2.1}$	$17.0^{+2.7}_{-2.0}$	0.21	1.98	-1.8×10^{-4}	2.6 ± 0.3

cross section for the ground state [34]. Therefore, we chose the density-independent interaction for simplicity.

The point-nucleon distribution of the ground state in ^{10}C was parametrized using the three-parameter Gaussian (3pG) function:

$$\rho(\boldsymbol{r}) = \frac{\rho_0 (1 + wr^2/c^2)}{1 + e^{(r^2-c^2)/z^2}}. \tag{6}$$

Here, c, z, and w are the parameters of the 3pG function. The normalization factor ρ_0 is determined so as to satisfy the relation

$$\int \rho(\boldsymbol{r})d\boldsymbol{r} = 4\pi \int \rho(\boldsymbol{r})r^2 dr = A, \tag{7}$$

where A is the mass number.

In standard analysis, the density distribution of the ground state is taken from the electron elastic scattering, and only the effective interaction is optimized to reproduce the alpha elastic scattering. However, the density distribution in ^{10}C is not known, and both the effective interaction and the density distribution must be determined simultaneously. Unfortunately, the effective interaction and the density distribution are not fully decoupled in the calculation of the cross section. The range parameter α in the effective interaction and the radius of the density distribution are strongly coupled; therefore, these parameters cannot be determined uniquely. In the present analysis, α was fixed at 2.13 fm. This value was determined by analyzing the $\alpha + ^{12}$C elastic scattering at 60 MeV/u [45] in the same manner as in Ref. [34].

The interaction parameters V and W and the 3pG parameters c, z, and w were optimized to reproduce the measured cross section of the $\alpha + ^{10}$C elastic scattering. The obtained parameters are listed in Table I, and the calculated cross section with these parameters is indicated by the solid line in Fig 8. The reduced chi-square of the fit, χ^2/ν, where ν is the number of degrees of freedom, is 4.98/5. The standard uncertainties of the parameters in the effective α-N interaction were estimated by varying one of the parameters over the range that satisfies the following relation:

$$\chi^2 \leqslant \chi^2_{\min} + 1. \tag{8}$$

When the uncertainty of one parameter was estimated, the other parameters were freely changed to minimize χ^2.

The deduced point-nucleon distribution of the ground state in ^{10}C is shown in Fig. 10. The vertical axis represents $\rho(r)$ multiplied by r^2. The distribution given by the best-fit parameters in Table I is drawn by the solid blue line with its error band. The error band was calculated by varying the three parameters in the 3pG function simultaneously over the range
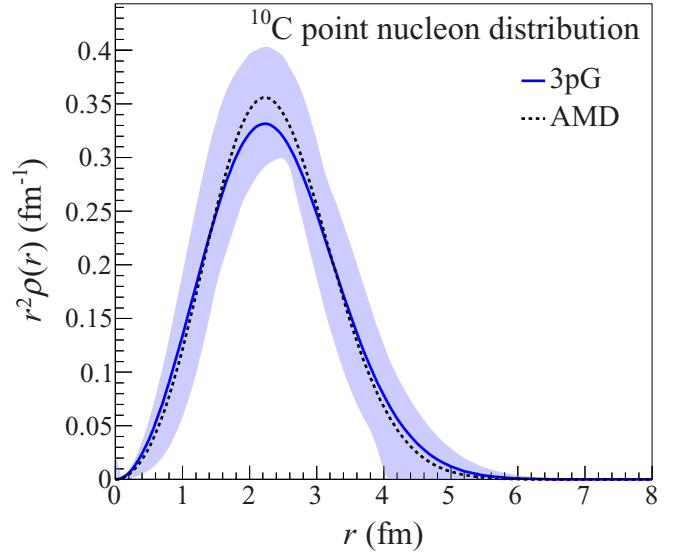

FIG. 10. Point-nucleon distribution of the ground state in ^{10}C. The density distribution obtained from the present work is shown by the solid blue line associated with the error band. The dashed black line represents the AMD calculation [47].

that satisfies

$$\chi^2 \leqslant \chi^2_{\min} + \Delta\chi^2. \tag{9}$$

When the error band was estimated, V and W in the effective interaction were freely changed to minimize χ^2. $\Delta\chi^2$ obeys the χ^2 distribution for three degrees of freedom since the 3pG function has three independent parameters [46]. Thus, $\Delta\chi^2$ is equal to 3.53 at a confidence level of 68.3%. Since the effective interaction and the density distribution were simultaneously optimized to reproduce the measured cross section in the present analysis, the deduced density distribution is associated with the large error band, as seen in Fig. 10.

The density distribution is compared with the theoretical one of the antisymmetrized molecular dynamics (AMD) model [47] plotted by the black dashed line. The present result is consistent with the AMD model. The root-mean-square (rms) radius of the point-nucleon distribution is 2.6 ± 0.3 fm, which is consistent with 2.42 ± 0.10 fm from the proton elastic scattering [13] and 2.52 fm from the AMD calculation; however, it is larger compared to 2.27 ± 0.03 fm, which is deduced from the interaction cross section [48].

B. Analysis of alpha inelastic scattering

The transition potential $\delta U(r)$ for the alpha inelastic scattering to the 2_1^+ state was obtained by folding the effective α-N interaction u with the transition density $\delta\rho(r)$:

$$\delta U(r) = \int \delta\rho(r)u[|\boldsymbol{r} - \boldsymbol{r}'|, \, \rho(\boldsymbol{r}')]d\boldsymbol{r}'. \tag{10}$$

The effective interaction was determined in Sec. IV A, and the transition density between the ground state and the 2_1^+ state was calculated by the macroscopic model [49]:

$$\delta\rho_{n(p)}(r) = -\delta_{n(p)} \frac{d}{dr}\rho_{n(p)}(r), \tag{11}$$

TABLE II. Experimental transition matrix elements of proton and neutron from the ground state to the 2_1^+ state in ^{10}C compared with theoretical calculations. The M_n/M_p ratios are also listed.

	M_p (fm^2)	M_n (fm^2)	M_n/M_p
Experiment	6.63 ± 0.11 [33]	6.9 ± 0.7 ± 1.2	1.05 ± 0.11 ± 0.17
Cluster [51]	5.5	4.4	0.8
No-core shell model [52]	5.3	5.7	1.1
Shell model [53]	3.3	4.3	1.3
Monte Carlo shell model [54]	6.8	6.8	1.0
AMD [55]	5.3	6.9	1.3

where $\delta_{n(p)}$ is the deformation length for a neutron (proton) and $\rho_{n(p)}(r)$ is the neutron (proton) density distribution in the ground state. Assuming that the proton and neutron distributions have the same shape, $\rho_p(r) = (Z/A)\rho(r)$ and $\rho_n(r) = (N/A)\rho(r)$ were used in the present analysis.

The transition matrix elements of neutron (proton) were calculated from the transition densities using the formula

$$M_{n(p)} = \int r^4 \delta \rho_{n(p)}(r) dr. \qquad (12)$$

Since a proton is not a pointlike particle in reality, its charge form factor should be taken into account when M_p is compared with $B(E2; 0_1^+ \rightarrow 2_1^+)$. However, the alteration due to the proton charge form factor is as low as a few percent, and it is negligible compared to other uncertainties in the present analysis. Once we assume a proton to be a point particle, the reduced electromagnetic transition rate $B(E2; 0_1^+ \rightarrow 2_1^+)$ is related to M_p by Eq. (2). The proton deformation length δ_p was determined so as to reproduce the known $B(E2; 0_1^+ \rightarrow 2_1^+)$ value of 44.0 ± 1.5 e^2fm^4 in ^{10}C [33]. The neutron deformation length δ_n was determined to reproduce the measured cross section of the inelastic alpha scattering as shown by the dashed line in Fig. 8. The result is $\delta_n = 2.4$ fm. From Eqs. (11) and (12), this corresponds to $M_n = 6.9$ fm^2. The reduced χ^2 of the fitting is $\chi^2/\nu = 10.9/7$.

The uncertainty of M_n from the procedure to fit the cross section of the inelastic scattering is ± 0.4 fm^2. The uncertainties of the interaction and 3pG parameters also cause an additional uncertainty in M_n. This uncertainty was estimated to be ± 0.6 fm^2 by propagating the uncertainty in those parameters into M_n. The total uncertainty from the procedures to fit the experimental data is ± 0.7 fm^2.

In Ref. [34], the transition matrix elements in stable self-conjugate even-even nuclei were obtained by analyzing cross sections from alpha inelastic scattering on the basis of DWBA calculations with single-folding potentials in a way similar to the present work. It was found that the matrix elements obtained by the inelastic alpha scattering erratically differ from the electromagnetic transition matrix elements taken from $B(E2; 0_1^+ \rightarrow 2_1^+)$ with a standard deviation of $\pm 17\%$. Thus, we adopt 17% (± 1.2 fm^2) as a systematic uncertainty due to the error in the DWBA analysis with single-folding potentials.

Finally, we obtained the M_n value in ^{10}C and its uncertainties as

$$M_n = 6.9 \pm 0.7 \, (\text{fit}) \pm 1.2 \, (\text{sys}) \, \text{fm}^2. \qquad (13)$$

V. DISCUSSION

The present result of M_n is larger than the previous result of $M_n = 5.51 \pm 1.09$ fm^2 determined by the proton inelastic scattering [13]. This discrepancy between the present and previous results is possibly because the authors in Ref. [13] used the old $B(E2; 0_1^+ \rightarrow 2_1^+)$ value from Ref. [32]. This old value of 61.5 ± 10 e^2fm^4 is larger than the new value of 44.0 ± 1.5 e^2fm^4 reported in Ref. [33]. We took the $B(E2; 0_1^+ \rightarrow 2_1^+)$ value from the recent measurement because of the smaller uncertainty. The larger $B(E2; 0_1^+ \rightarrow 2_1^+)$ value might lead to a smaller value of M_n. If we take the old $B(E2; 0_1^+ \rightarrow 2_1^+)$ value, the M_n value becomes $M_n = 5.7 \pm 0.6 \, (\text{fit}) \pm 1.0 \, (\text{sys})$ fm^2. This value is consistent with the previous result.

Assuming charge symmetry in the $A = 10$ system, M_n in ^{10}C should be equal to M_p in ^{10}Be. M_p in ^{10}Be is reported as 6.78 ± 0.11 fm^2 [50]. This value is actually close to the present M_n value in ^{10}C, and thus charge symmetry in the $A = 10$ system is almost conserved.

The M_n/M_p ratio in ^{10}C deduced from the present measurement is

$$M_n/M_p = 1.05 \pm 0.11 \, (\text{fit}) \pm 0.17 \, (\text{sys}). \qquad (14)$$

The transition from the ground state to the 2_1^+ state in ^{10}C is almost isoscalar, whereas a large M_n/M_p ratio of 3.2 ± 0.7 was reported in ^{16}C [20]. This indicates that the quadrupole transition in ^{10}C is less neutron dominant compared to that in ^{16}C. The M_n/M_p value close to unity in ^{10}C shows that the effect of the $Z = 6$ subshell closure is less evident compared to the neutron-rich side.

The present results are compared with the theoretical predictions by the $2p + 2\alpha$ four-body cluster model [51], no-core shell model [52], shell model [53], Monte Carlo shell model [54], and AMD model [55] in Table II. In the cluster-model calculation, fully antisymmetrized ten-nucleon wave functions were built in a microscopic $2p + 2\alpha$ configuration space using the Minnesota interaction [56]. The no-core shell model calculation was performed using the CD-Bonn NN potential in the basis space up to $8\hbar\Omega$ with the harmonic oscillator frequency of $\hbar\Omega = 14$ MeV. The shell-model calculation was conducted within the p shell using the Cohen and Kurath (8–16)2BME interaction [57]. The shell-model transition matrix elements were calculated using single-particle wave functions in the harmonic oscillator potential with $b = 1.64$ fm and effective charges of $e_p = 1.3e$ and $e_n = 0.5e$. In the Monte Carlo shell-model calculation, the unitary correlation operator method potential based on the chiral

next-to-next-to-next-to-leading-order two nucleon interaction [58] with the bare charges ($e_p = e$ and $e_n = 0$) was used to calculate the transition matrix elements. The M_n value in ^{10}C from the Monte Carlo shell-model calculation was taken from the M_p value in the mirror nucleus ^{10}Be assuming charge symmetry.

Theoretical calculations systematically underestimate M_p and M_n, except for the Monte Carlo shell-model calculation and M_n calculated by the AMD model. Especially, M_p and M_n predicted by the shell-model calculation are considerably smaller than the experiment. However, the M_n/M_p ratios from the theoretical calculations are close to unity, supporting the present result that enhancement of the M_n/M_p, which was observed in neutron-rich ^{16}C, was not observed in proton-rich ^{10}C.

VI. SUMMARY

Alpha elastic and inelastic scatterings from ^{10}C at 68 MeV/u were measured under the inverse kinematic condition at RCNP, Osaka University. The purity and intensity of the ^{10}C secondary beam were 96% and 70 kcps, respectively. The recoil alpha particles were detected using the newly developed MAIKo active target system [35]. This system enabled the detection of low-energy recoil alpha particles down to $E_\alpha = 0.5$ MeV, which corresponds to momentum transfer down to $q = 0.4$ fm^{-1}. The excitation-energy resolution was approximately 1 MeV in sigma, sufficient to distinguish the first excited 2_1^+ state at $E_x = 3.35$ MeV from the ground state in ^{10}C.

The cross section for the $\alpha + ^{12}$C elastic scattering was also measured using a primary ^{12}C beam at 94 MeV/u. The measured cross section was compared with the previous result obtained under the normal kinematic condition using a ^{4}He beam at 96 MeV/u [34], and we confirmed that both results are qualitatively consistent.

The cross section of the $\alpha + ^{10}$C elastic scattering enabled the determination of the phenomenological α-N effective interaction and the point-nucleon distribution of the ground state in ^{10}C. The rms radius of 2.6 ± 0.3 fm in ^{10}C is consistent with the theoretical prediction by the AMD calculation [47] and the experimental result of the previous proton elastic scattering [13], but slightly larger than that deduced from the interaction cross section [48].

From the cross section of the $\alpha + ^{10}$C inelastic scattering to the 2_1^+ state, the neutron transition matrix element of $M_n = 6.9 \pm 0.7$ (fit) ± 1.2 (sys) was obtained. The M_n/M_p ratio in ^{10}C was determined as $M_n/M_p = 1.05 \pm 0.11$ (fit) ± 0.17 (sys), and thus the effect of the $Z = 6$ subshell closure reported in neutron-rich carbon isotopes [31] is not evident in the proton-rich side. This result is supported from the theoretical calculations.

The first physics experiment using the MAIKo active target was successfully completed. MAIKo will be employed in various RI beam experiments in the near future.

[1] A. M. Bernstein, V. R. Brown, and V. A. Madsen, Phys. Rev. Lett. **42**, 425 (1979).

[2] A. Bernstein, V. Brown, and V. Madsen, Phys. Lett. B **103**, 255 (1981).

[3] A. M. Bernstein, V. R. Brown, and V. A. Madsen, Comments Nucl. Part. Phys. **11**, 203 (1983).

[4] M. A. Kennedy, P. D. Cottle, and K. W. Kemper, Phys. Rev. C **46**, 1811 (1992).

[5] K. H. Bhatt, C. W. Nestor, and S. Raman, Phys. Rev. C **46**, 164 (1992).

[6] L. A. Riley, J. K. Jewell, P. D. Cottle, T. Glasmacher, K. W. Kemper, N. Alamanos, Y. Blumenfeld, J. A. Carr, M. J. Chromik, R. W. Ibbotson, F. Maréchal, W. E. Ormand, F. Petrovich, H. Scheit, and T. Suomijärvi, Phys. Rev. Lett. **82**, 4196 (1999).

[7] J. K. Jewell, L. A. Riley, P. D. Cottle, K. W. Kemper, T. Glasmacher, R. W. Ibbotson, H. Scheit, M. Chromik, Y. Blumenfeld, S. E. Hirzebruch, F. Maréchal, and T. Suomijärvi, Phys. Lett. B **454**, 181 (1999).

[8] H. Iwasaki, T. Motobayashi, H. Akiyoshi, Y. Ando, N. Fukuda, H. Fujiwara, Z. Fülöp, K. I. Hahn, Y. Higurashi, M. Hirai, I. Hisanaga, N. Iwasa, T. Kijima, T. Minemura, T. Nakamura, M. Notani, S. Ozawa, H. Sakurai, S. Shimoura, S. Takeuchi, T.

Teranishi, Y. Yanagisawa, and M. Ishihara, Phys. Lett. B **481**, 7 (2000).

[9] E. Khan, T. Suomijärvi, Y. Blumenfeld, N. Van Giai, N. Alamanos, F. Auger, E. Bauge, D. Beaumel, J. P. Delaroche, P. Delbourgo-Salvador, A. Drouart, S. Fortier, N. Frascaria, A. Gillibert, M. Girod, C. Jouanne, K. W. Kemper, A. Lagoyannis, V. Lapoux, A. Lépine-Szily, I. Lhenry, J. Libert, F. Maréchal, J. M. Maison, A. Musumarra, S. Ottini-Hustache, P. Piattelli, S. Pita, E. C. Pollacco, P. Roussel-Chomaz, D. Santonocito, J. E. Sauvestre, J. A. Scarpaci, and T. Zerguerras, Nucl. Phys. A **694**, 103 (2001).

[10] P. D. Cottle, Z. Hu, B. V. Pritychenko, J. A. Church, M. Fauerbach, T. Glasmacher, R. W. Ibbotson, K. W. Kemper, L. A. Riley, H. Scheit, and M. Steiner, Phys. Rev. Lett. **88**, 172502 (2002).

[11] Z. Elekes, Z. Dombrádi, A. Krasznahorkay, H. Baba, M. Csatlós, L. Csige, N. Fukuda, Z. Fülöp, Z. Gácsi, J. Gulyás, N. Iwasa, H. Kinugawa, S. Kubono, M. Kurokawa, X. Liu, S. Michimasa, T. Minemura, T. Motobayashi, A. Ozawa, A. Saito, S. Shimoura, S. Takeuchi, I. Tanihata, P. Thirolf, Y. Yanagisawa, and K. Yoshida, Phys. Lett. B **586**, 34 (2004).

[12] N. Imai, H. J. Ong, N. Aoi, H. Sakurai, K. Demichi, H. Kawasaki, H. Baba, Z. Dombrádi, Z. Elekes, N. Fukuda,

Z. Fülöp, A. Gelberg, T. Gomi, H. Hasegawa, K. Ishikawa, H. Iwasaki, E. Kaneko, S. Kanno, T. Kishida, Y. Kondo, T. Kubo, K. Kurita, S. Michimasa, T. Minemura, M. Miura, T. Motobayashi, T. Nakamura, M. Notani, T. K. Onishi, A. Saito, S. Shimoura, T. Sugimoto, M. K. Suzuki, E. Takeshita, S. Takeuchi, M. Tamaki, K. Yamada, K. Yoneda, H. Watanabe, and M. Ishihara, Phys. Rev. Lett. **92**, 062501 (2004).

[13] C. Jouanne, V. Lapoux, F. Auger, N. Alamanos, A. Drouart, A. Gillibert, G. Lobo, A. Musumarra, L. Nalpas, E. Pollacco, J.-L. Sida, M. Trotta, Y. Blumenfeld, E. Khan, T. Suomijärvi, T. Zerguerras, P. Roussel-Chomaz, H. Savajols, A. Lagoyannis, and A. Pakou, Phys. Rev. C **72**, 014308 (2005).

[14] L. A. Riley, M. A. Abdelqader, D. Bazin, M. J. Bojazi, B. A. Brown, C. M. Campbell, J. A. Church, P. D. Cottle, D. C. Dinca, J. Enders, A. Gade, T. Glasmacher, M. Honma, S. Horibe, Z. Hu, K. W. Kemper, W. F. Mueller, H. Olliver, T. Otsuka, B. C. Perry, B. T. Roeder, B. M. Sherrill, T. P. Spencer, and J. R. Terry, Phys. Rev. C **72**, 024311 (2005).

[15] K. Yamada, T. Motobayashi, N. Aoi, H. Baba, K. Demichi, Z. Elekes, J. Gibelin, T. Gomi, H. Hasegawa, N. Imai, H. Iwasaki, S. Kanno, T. Kubo, K. Kurita, Y. Matsuyama, S. Michimasa, T. Minemura, M. Notani, T. Onishi K., H.J. Ong, S. Ota, A. Ozawa, A. Saito, H. Sakurai, S. Shimoura, E. Takeshita, S. Takeuchi, M. Tamaki, Y. Togano, Y. Yanagisawa, K. Yoneda, and I. Tanihata, Eur. Phys. J. A **25**, 409 (2005).

[16] H. J. Ong, N. Imai, N. Aoi, H. Sakurai, Z. Dombrádi, A. Saito, Z. Elekes, H. Baba, K. Demichi, Z. S. Fülöp, J. Gibelin, T. Gomi, H. Hasegawa, M. Ishihara, H. Iwasaki, S. Kanno, S. Kawai, T. Kubo, K. Kurita, Y. U. Matsuyama, S. Michimasa, T. Minemura, T. Motobayashi, M. Notani, S. Ota, H. K. Sakai, S. Shimoura, E. Takeshita, S. Takeuchi, M. Tamaki, Y. Togano, K. Yamada, Y. Yanagisawa, and K. Yoneda, Phys. Rev. C **73**, 024610 (2006).

[17] E. Becheva, Y. Blumenfeld, E. Khan, D. Beaumel, J. M. Daugas, F. Delaunay, C.-E. Demonchy, A. Drouart, M. Fallot, A. Gillibert, L. Giot, M. Grasso, N. Keeley, K. W. Kemper, D. T. Khoa, V. Lapoux, V. Lima, A. Musumarra, L. Nalpas, E. C. Pollacco, O. Roig, P. Roussel-Chomaz, J. E. Sauvestre, J. A. Scarpaci, F. Skaza, and H. S. Than, Phys. Rev. Lett. **96**, 012501 (2006).

[18] C. M. Campbell, N. Aoi, D. Bazin, M. D. Bowen, B. A. Brown, J. M. Cook, D. C. Dinca, A. Gade, T. Glasmacher, M. Horoi, S. Kanno, T. Motobayashi, L. A. Riley, H. Sagawa, H. Sakurai, K. Starosta, H. Suzuki, S. Takeuchi, J. R. Terry, K. Yoneda, and H. Zwahlen, Phys. Lett. B **652**, 169 (2007).

[19] M. Wiedeking, P. Fallon, A. O. Macchiavelli, J. Gibelin, M. S. Basunia, R. M. Clark, M. Cromaz, M.-A. Deleplanque, S. Gros, H. B. Jeppesen, P. T. Lake, I.-Y. Lee, L. G. Moretto, J. Pavan, L. Phair, E. Rodriguez-Vietiez, F. S. Stephens, L. A. Bernstein, D. L. Bleuel, J. T. Burke, S. R. Lesher, B. F. Lyles, and N. D. Scielzo, Phys. Rev. Lett. **100**, 152501 (2008).

[20] H. J. Ong, N. Imai, D. Suzuki, H. Iwasaki, H. Sakurai, T. K. Onishi, M. K. Suzuki, S. Ota, S. Takeuchi, T. Nakao, Y. Togano, Y. Kondo, N. Aoi, H. Baba, S. Bishop, Y. Ichikawa, M. Ishihara, T. Kubo, K. Kurita, T. Motobayashi, T. Nakamura, T. Okumura, and Y. Yanagisawa, Phys. Rev. C **78**, 014308 (2008).

[21] Z. Elekes, Z. Dombrádi, T. Aiba, N. Aoi, H. Baba, D. Bemmerer, B. A. Brown, T. Furumoto, Z. Fülöp, N. Iwasa, Á. Kiss, T. Kobayashi, Y. Kondo, T. Motobayashi, T. Nakabayashi, T. Nannichi, Y. Sakuragi, H. Sakurai, D. Sohler,

M. Takashina, S. Takeuchi, K. Tanaka, Y. Togano, K. Yamada, M. Yamaguchi, and K. Yoneda, Phys. Rev. C **79**, 011302 (2009).

[22] M. Petri, P. Fallon, A. O. Macchiavelli, S. Paschalis, K. Starosta, T. Baugher, D. Bazin, L. Cartegni, R. M. Clark, H. L. Crawford, M. Cromaz, A. Dewald, A. Gade, G. F. Grinyer, S. Gros, M. Hackstein, H. B. Jeppesen, I. Y. Lee, S. McDaniel, D. Miller, M. M. Rajabali, A. Ratkiewicz, W. Rother, P. Voss, K. A. Walsh, D. Weisshaar, M. Wiedeking, and B. A. Brown, Phys. Rev. Lett. **107**, 102501 (2011).

[23] M. Petri, S. Paschalis, R. M. Clark, P. Fallon, A. O. Macchiavelli, K. Starosta, T. Baugher, D. Bazin, L. Cartegni, H. L. Crawford, M. Cromaz, U. Datta Pramanik, G. de Angelis, A. Dewald, A. Gade, G. F. Grinyer, S. Gros, M. Hackstein, H. B. Jeppesen, I. Y. Lee, S. McDaniel, D. Miller, M. M. Rajabali, A. Ratkiewicz, W. Rother, P. Voss, K. A. Walsh, D. Weisshaar, M. Wiedeking, B. A. Brown, C. Forssén, P. Navrátil, and R. Roth, Phys. Rev. C **86**, 044329 (2012).

[24] P. Voss, T. Baugher, D. Bazin, R. M. Clark, H. L. Crawford, A. Dewald, P. Fallon, A. Gade, G. F. Grinyer, H. Iwasaki, A. O. Macchiavelli, S. McDaniel, D. Miller, M. Petri, A. Ratkiewicz, W. Rother, K. Starosta, K. A. Walsh, D. Weisshaar, C. Forssén, R. Roth, and P. Navrátil, Phys. Rev. C **86**, 011303 (2012).

[25] Y. Togano, Y. Yamada, N. Iwasa, K. Yamada, T. Motobayashi, N. Aoi, H. Baba, S. Bishop, X. Cai, P. Doornenbal, D. Fang, T. Furukawa, K. Ieki, T. Kawabata, S. Kanno, N. Kobayashi, Y. Kondo, T. Kuboki, N. Kume, K. Kurita, M. Kurokawa, Y. G. Ma, Y. Matsuo, H. Murakami, M. Matsushita, T. Nakamura, K. Okada, S. Ota, Y. Satou, S. Shimoura, R. Shioda, K. N. Tanaka, S. Takeuchi, W. Tian, H. Wang, J. Wang, and K. Yoneda, Phys. Rev. Lett. **108**, 222501 (2012).

[26] S. Michimasa, Y. Yanagisawa, K. Inafuku, N. Aoi, Z. Elekes, Z. Fülöp, Y. Ichikawa, N. Iwasa, K. Kurita, M. Kurokawa, T. Machida, T. Motobayashi, T. Nakamura, T. Nakabayashi, M. Notani, H. J. Ong, T. K. Onishi, H. Otsu, H. Sakurai, M. Shinohara, T. Sumikama, S. Takeuchi, K. Tanaka, Y. Togano, K. Yamada, M. Yamaguchi, and K. Yoneda, Phys. Rev. C **89**, 054307 (2014).

[27] L. A. Riley, M. L. Agiorgousis, T. R. Baugher, D. Bazin, M. Bowry, P. D. Cottle, F. G. DeVone, A. Gade, M. T. Glowacki, K. W. Kemper, E. Lunderberg, D. M. McPherson, S. Noji, F. Recchia, B. V. Sadler, M. Scott, D. Weisshaar, and R. G. T. Zegers, Phys. Rev. C **90**, 011305 (2014).

[28] A. Corsi, S. Boissinot, A. Obertelli, P. Doornenbal, M. Dupuis, F. Lechaftois, M. Matsushita, S. Péru, S. Takeuchi, H. Wang, N. Aoi, H. Baba, P. Bednarczyk, M. Ciemala, A. Gillibert, T. Isobe, A. Jungclaus, V. Lapoux, J. Lee, M. Martini, K. Matsui, T. Motobayashi, D. Nishimura, S. Ota, E. Pollacco, H. Sakurai, C. Santamaria, Y. Shiga, D. Sohler, D. Steppenbeck, and R. Taniuchi, Phys. Lett. B **743**, 451 (2015).

[29] M. L. Cortés, P. Doornenbal, M. Dupuis, S. M. Lenzi, F. Nowacki, A. Obertelli, S. Péru, N. Pietralla, V. Werner, K. Wimmer, G. Authelet, H. Baba, D. Calvet, F. Château, A. Corsi, A. Delbart, J.-M. Gheller, A. Gillibert, T. Isobe, V. Lapoux, C. Louchart, M. Matsushita, S. Momiyama, T. Motobayashi, M. Niikura, H. Otsu, C. Péron, A. Peyaud, E. C. Pollacco, J.-Y. Roussé, H. Sakurai, C. Santamaria, M. Sasano, Y. Shiga, S. Takeuchi, R. Taniuchi, T. Uesaka, H. Wang, K. Yoneda, F. Browne, L. X. Chung, Z. Dombradi, S. Franchoo, F. Giacoppo, A. Gottardo, K. Hadynska-Klek, Z. Korkulu, S. Koyama, Y. Kubota, J. Lee, M. Lettmann, R. Lozeva, K. Matsui, T. Miyazaki, S. Nishimura, L. Olivier, S. Ota, Z. Patel, E. Sahin,

C. M. Shand, P.-A. Söderström, I. Stefan, D. Steppenbeck, T. Sumikama, D. Suzuki, Z. Vajta, J. Wu, and Z. Xu, Phys. Rev. C **97**, 044315 (2018).

[30] L. A. Riley, D. Bazin, J. Belarge, P. C. Bender, B. A. Brown, P. D. Cottle, B. Elman, A. Gade, S. D. Gregory, E. B. Haldeman, K. W. Kemper, B. R. Klybor, M. A. Liggett, S. Lipschutz, B. Longfellow, E. Lunderberg, T. Mijatovic, J. Pereira, L. M. Skiles, R. Titus, A. Volya, D. Weisshaar, J. C. Zamora, and R. G. T. Zegers, Phys. Rev. C **100**, 044312 (2019).

[31] D. T. Tran, H. J. Ong, G. Hagen, T. D. Morris, N. Aoi, T. Suzuki, Y. Kanada-En'yo, L. S. Geng, S. Terashima, I. Tanihata, T. T. Nguyen, Y. Ayyad, P. Y. Chan, M. Fukuda, H. Geissel, M. N. Harakeh, T. Hashimoto, T. H. Hoang, E. Ideguchi, A. Inoue, G. R. Jansen, R. Kanungo, T. Kawabata, L. H. Khiem, W. P. Lin, K. Matsuta, M. Mihara, S. Momota, D. Nagae, N. D. Nguyen, D. Nishimura, T. Otsuka, A. Ozawa, P. P. Ren, H. Sakaguchi, C. Scheidenberger, J. Tanaka, M. Takechi, R. Wada, and T. Yamamoto, Nat. Commun. **9**, 1594 (2018).

[32] T. R. Fisher, S. S. Hanna, D. C. Healey, and P. Paul, Phys. Rev. **176**, 1130 (1968).

[33] E. A. McCutchan, C. J. Lister, S. C. Pieper, R. B. Wiringa, D. Seweryniak, J. P. Greene, P. F. Bertone, M. P. Carpenter, C. J. Chiara, G. Gürdal, C. R. Hoffman, R. V. F. Janssens, T. L. Khoo, T. Lauritsen, and S. Zhu, Phys. Rev. C **86**, 014312 (2012).

[34] S. Adachi, T. Kawabata, K. Minomo, T. Kadoya, N. Yokota, H. Akimune, T. Baba, H. Fujimura, M. Fujiwara, Y. Funaki, T. Furuno, T. Hashimoto, K. Hatanaka, K. Inaba, Y. Ishii, M. Itoh, C. Iwamoto, K. Kawase, Y. Maeda, H. Matsubara, Y. Matsuda, H. Matsuno, T. Morimoto, H. Morita, M. Murata, T. Nanamura, I. Ou, S. Sakaguchi, Y. Sasamoto, R. Sawada, Y. Shimizu, K. Suda, A. Tamii, Y. Tameshige, M. Tsumura, M. Uchida, T. Uesaka, H. P. Yoshida, and S. Yoshida, Phys. Rev. C **97**, 014601 (2018).

[35] T. Furuno, T. Kawabata, H. J. Ong, S. Adachi, Y. Ayyad, T. Baba, Y. Fujikawa, T. Hashimoto, K. Inaba, Y. Ishii, S. Kabuki, H. Kubo, Y. Matsuda, Y. Matsuoka, T. Mizumoto, T. Morimoto, M. Murata, T. Sawano, T. Suzuki, A. Takada, J. Tanaka, I. Tanihata, T. Tanimori, D. T. Tran, M. Tsumura, and H. D. Watanabe, Nucl. Instrum. Methods Phys. Res. A **908**, 215 (2018).

[36] T. Shimoda, H. Miyatake, and S. Morinobu, Nucl. Instrum. Methods Phys. Res. B **70**, 320 (1992).

[37] S. Mitsuoka, T. Shimoda, H. Miyatake, Y. Mizoi, H. Kobayashi, M. Sasaki, T. Shirakura, N. Takahashi, T. Murakami, and S. Morinobu, Nucl. Instrum. Methods Phys. Res. A **372**, 489 (1996).

[38] H. J. Ong, in *Frontiers in Physics: 4th International Meeting, 27–30 August 2013, Kuala Lumpur*, edited by K. Ratnavelu, S.-P. Chia, C. S. Wong, and R.C.-H. Ooi, AIP Conf. Proc. No. 1588 (AIP, New York, 2014), p. 146.

[39] A. Ochi, T. Nagayoshi, S. Koishi, T. Tanimori, T. Nagae, and M. Nakamura, Nucl. Instrum. Methods Phys. Res. A **471**, 264 (2001).

[40] T. Mizumoto, Y. Matsuoka, Y. Mizumura, T. Tanimori, H. Kubo, A. Takada, S. Iwaki, T. Sawano, K. Nakamura, S. Komura, S. Nakamura, T. Kishimoto, M. Oda, S. Miyamoto, T. Takemura, J. Parker, D. Tomono, S. Sonoda, K. Miuchi, and S. Kurosawa, Nucl. Instrum. Methods Phys. Res. A **800**, 40 (2015).

[41] P. Hough, in *2nd International Conference on High-Energy Accelerators and Instrumentation* (CERN, Geneva, 1959), p. 554.

[42] R. O. Duda and P. E. Hart, Commun. ACM **15**, 11 (1972).

[43] J. Ziegler, M. Ziegler, and J. Biersack, Nucl. Instrum. Methods Phys. Res. B **268**, 1818 (2010).

[44] J. Raynal, computer program ECIS-95, Nuclear Energy Agency Report No. NEA-0850/19 (unpublished).

[45] B. John, Y. Tokimoto, Y.-W. Lui, H. L. Clark, X. Chen, and D. H. Youngblood, Phys. Rev. C **68**, 014305 (2003).

[46] P. R. Bevington and D. K. Robinson, *Data Reduction and Error Analysis for the Physical Sciences* (McGraw-Hill, New York, 2003).

[47] Y. Kanada-En'yo, Phys. Rev. C **91**, 014315 (2015).

[48] A. Ozawa, I. Tanihata, T. Kobayashi, Y. Sugahara, O. Yamakawa, K. Omata, K. Sugimoto, D. Olson, W. Christie, and H. Wieman, Nucl. Phys. A **608**, 63 (1996).

[49] G. Satchler, Nucl. Phys. A **472**, 215 (1987).

[50] E. A. McCutchan, C. J. Lister, R. B. Wiringa, S. C. Pieper, D. Seweryniak, J. P. Greene, M. P. Carpenter, C. J. Chiara, R. V. F. Janssens, T. L. Khoo, T. Lauritsen, I. Stefanescu, and S. Zhu, Phys. Rev. Lett. **103**, 192501 (2009).

[51] Y. Ogawa, K. Arai, Y. Suzuki, and K. Varga, Nucl. Phys. A **673**, 122 (2000).

[52] E. Caurier, P. Navrátil, W. E. Ormand, and J. P. Vary, Phys. Rev. C **66**, 024314 (2002).

[53] H. Sagawa, X. R. Zhou, X. Z. Zhang, and T. Suzuki, Phys. Rev. C **70**, 054316 (2004).

[54] L. Liu, T. Otsuka, N. Shimizu, Y. Utsuno, and R. Roth, Phys. Rev. C **86**, 014302 (2012).

[55] Y. Kanada-En'yo, Phys. Rev. C **84**, 024317 (2011).

[56] D. Thompson, M. Lemere, and Y. Tang, Nucl. Phys. A **286**, 53 (1977).

[57] S. Cohen and D. Kurath, Nucl. Phys. **73**, 1 (1965).

[58] R. Machleidt and D. R. Entem, Phys. Rep. **503**, 1 (2011).